

# A $5 \times 10^9 M_{\odot}$ BLACK HOLE IN NGC 1277 FROM ADAPTIVE OPTICS SPECTROSCOPY

JONELLE L. WALSH<sup>1</sup>, REMCO C. E. VAN DEN BOSCH<sup>2</sup>, KARL GEBHARDT<sup>3</sup>, AKIN YILDIRIM<sup>2</sup>, DOUGLAS O. RICHSTONE<sup>4</sup>, KAYHAN GÜLTEKIN<sup>4</sup>, AND BERND HUSEMANN<sup>5</sup>

<sup>1</sup> George P. and Cynthia Woods Mitchell Institute for Fundamental Physics and Astronomy, Department of Physics and Astronomy, Texas A&M University, College Station, TX 77843, USA; walsh@physics.tamu.edu

<sup>2</sup> Max-Planck Institut für Astronomie, Königstuhl 17, D-69117 Heidelberg, Germany

<sup>3</sup> Department of Astronomy, The University of Texas at Austin, 2515 Speedway, Stop C1400, Austin, TX 78712, USA

<sup>4</sup> Department of Astronomy, University of Michigan, 1085 S. University Ave., Ann Arbor, MI 48109, USA

<sup>5</sup> European Southern Observatory, Karl-Schwarzschild-Str. 2, 85748 Garching, Germany

*Draft version November 17, 2015*

## ABSTRACT

The nearby lenticular galaxy NGC 1277 is thought to host one of the largest black holes known, however the black hole mass measurement is based on low spatial resolution spectroscopy. In this paper, we present Gemini Near-infrared Integral Field Spectrometer observations assisted by adaptive optics. We map out the galaxy's stellar kinematics within  $\sim 440$  pc of the nucleus with an angular resolution that allows us to probe well within the region where the potential from the black hole dominates. We find that the stellar velocity dispersion rises dramatically, reaching  $\sim 550$  km s<sup>-1</sup> at the center. Through orbit-based, stellar-dynamical models we obtain a black hole mass of  $(4.9 \pm 1.6) \times 10^9 M_{\odot}$  ( $1\sigma$  uncertainties). Although the black hole mass measurement is smaller by a factor of  $\sim 3$  compared to previous claims based on large-scale kinematics, NGC 1277 does indeed contain one of the most massive black holes detected to date, and the black hole mass is an order of magnitude larger than expectations from the empirical relation between black hole mass and galaxy luminosity. Given the galaxy's similarities to the higher redshift ( $z \sim 2$ ) massive quiescent galaxies, NGC 1277 could be a relic, passively evolving since that period. A population of local analogs to the higher redshift quiescent galaxies that also contain over-massive black holes may suggest that black hole growth precedes that of the host galaxy.

*Subject headings:* galaxies: elliptical and lenticular, cD – galaxies: individual (NGC 1277) – galaxies: kinematics and dynamics – galaxies: nuclei – black hole physics

## 1. INTRODUCTION

The relationships between black hole mass,  $M_{\text{BH}}$ , and large-scale host galaxy properties, such as bulge luminosity,  $L_{\text{bul}}$ , and stellar velocity dispersion,  $\sigma_*$  (e.g., Kormendy & Richstone 1995; Ferrarese & Merritt 2000; Gebhardt et al. 2000; Marconi & Hunt 2003; Gültekin et al. 2009) suggest that black holes play a fundamental role in the evolution of galaxies. It is believed that supermassive black holes and galaxies grow in tandem, with the black hole governing the properties of galaxies through feedback mechanisms (Silk & Rees 1998; Fabian 1999). However, the scaling relations can also be established without black hole feedback, simply owing to the inherent averaging of properties that accompanies galaxy mergers (Peng 2007; Jahnke & Macciò 2011). The main physical process that drives the black hole-galaxy relations remains poorly understood and it is unclear how important feedback-driven co-evolution is compared to a non-causal link associated with merger averaging (e.g., Kormendy & Ho 2013). A better understanding of the role that black holes play in galaxy evolution requires increasing the number of  $M_{\text{BH}}$  measurements, especially for low and high-mass black holes and over a larger range of galaxy types/properties.

NGC 1277 is thought to harbor one of the most massive black holes in the Universe (van den Bosch et al. 2012). The nearby lenticular galaxy is a flattened, fast rotator with a cuspy surface brightness profile. Of the  $\sim 80$  dynamical black hole mass measurements currently on the black hole-galaxy relations (McConnell & Ma 2013; Kormendy & Ho 2013), NGC 1277 shares the most similarities with NGC 4342

(Cretton & van den Bosch 1999), NGC 1332 (Rusli et al. 2011), and NGC 1271 (Walsh et al. 2015). All of these early-type galaxies are significant positive outliers from the  $M_{\text{BH}} - L_{\text{bul}}$  relation (by at least  $2\sigma$ ), and have small sizes (effective radii,  $R_e$ , below 3 kpc) and large stellar velocity dispersions ( $225 - 333$  km s<sup>-1</sup>) for their  $K$ -band luminosities ( $2.7 \times 10^{10} - 1.6 \times 10^{11} L_{\odot}$ ). NGC 4486B (Kormendy et al. 1997) and M60-UCD1 (Seth et al. 2014) are also extreme outliers from  $M_{\text{BH}} - L_{\text{bul}}$  with small sizes and elevated velocity dispersions for their galaxy luminosities.

The compact, high-dispersion galaxies like NGC 1277 are distinct from the typical giant elliptical galaxies and Brightest Cluster Galaxies (BCGs) that are expected to contain the largest black holes and occupy the upper end of the black hole-galaxy relationships. Giant ellipticals and BCGs instead have large sizes, surface brightness profiles with flat central cores, are pressure supported, and often are slow rotators (Dalla Bontà et al. 2009; McConnell et al. 2012). Therefore measuring black hole masses in the compact, high-dispersion galaxies and the giant ellipticals/BCGs is helpful for searching for systematic deviations in the black hole scaling relationships between the two kinds of early-type galaxies. If such differences arise, this would suggest that the black holes and galaxies grew in different manners.

Galaxies like NGC 1277, however, appear remarkably similar to the higher redshift massive quiescent galaxies. The  $z \sim 2$  quiescent galaxies are also small, have large velocity dispersions, exhibit disk structures (e.g., Daddi et al. 2005; Trujillo et al. 2006; van Dokkum et al. 2009; van der Wel et al. 2011), and are thought to grow into the present-day massive galaxies through a series of merg-

ers (e.g., van Dokkum et al. 2010; Wellons et al. 2015). Given the resemblance to the  $z \sim 2$  red nuggets, the compact, high-dispersion galaxies could be relics that followed a different pathway than the local massive galaxies, instead experiencing passive evolution (Trujillo et al. 2014; Ferré-Mateu et al. 2015). If galaxies like NGC 1277 are local analogs of the  $z \sim 2$  quiescent galaxies and continue to show evidence for harboring over-massive black holes, then such galaxies may reflect a previous period when the local black hole scaling relations did not apply. Instead, galaxies may have contained over-massive black holes at higher redshifts, suggesting that black hole growth precedes that of its host galaxy. Indeed there could be hints that black holes at higher redshifts (masses estimated in active galactic nuclei through the width of broad emission lines) are over-massive at fixed galaxy mass compared to the local relation (e.g., Peng et al. 2006; Woo et al. 2008; Merloni et al. 2010; Decarli et al. 2010; Bennert et al. 2011; Trakhtenbrot et al. 2015), however there are also a number of studies that find essentially no change in the black hole scaling relations with redshift (e.g., Salviander & Shields 2013; Salviander et al. 2015; Shen et al. 2015) and selection bias can lead to the false identification of evolution in  $M_{\text{BH}} - \sigma_*$  and  $M_{\text{BH}} - L_{\text{bul}}$  (Lauer et al. 2007; Schulze & Wisotzki 2014).

The black hole in NGC 1277 has several previous  $M_{\text{BH}}$  measurements. van den Bosch et al. (2012) first reported the presence of a  $1.7 \times 10^{10} M_{\odot}$  black hole using stellar-dynamical models and a long-slit spectroscopic observation from the Hobby-Eberly Telescope (HET) at McDonald Observatory. The total stellar mass of NGC 1277 is  $1.2 \times 10^{11} M_{\odot}$ , and therefore the ratio between black hole mass and galaxy stellar mass is surprisingly high at 14%. van den Bosch et al. (2012) also listed another five galaxies found through the HET Massive Galaxy Survey (van den Bosch et al. 2015) that could host similarly large black holes. Such an extraordinary black hole mass for NGC 1277, however, was called into question by Emsellem (2013), who compared dynamical models from N-body realizations to the same HET kinematics. Emsellem (2013) did not search for a best-fit model, but demonstrated that a  $5 \times 10^9 M_{\odot}$  black hole was sufficient to reproduce the observed kinematics, with the exception of the central  $h_4$  measurements. More recently, Yildirim et al. (2015) used integral-field unit (IFU) observations from the 3.5m telescope at Calar Alto Observatory and orbit-based dynamical models to confirm the mass measurement of van den Bosch et al. (2012), although they extend the bound of the uncertainty on the black hole mass measurement to possibly as low as  $4.0 \times 10^9 M_{\odot}$ .

While the above black hole mass determinations were made from analyzing the stellar kinematics of NGC 1277, gas kinematics can also be used constrain  $M_{\text{BH}}$ . Scharwächter et al. (2015) presented the detection of cold molecular gas arising from the nuclear dust disk based on IRAM Plateau de Bure Interferometer (PdBI) observations. The CO(1-0) emission was spatially unresolved, but the double-horned profile suggested an enclosed mass of  $\sim 2 \times 10^{10} M_{\odot}$ . Depending on the stellar mass-to-light ratio assumed, both a  $\sim 1.7 \times 10^{10} M_{\odot}$  or a  $\sim 5 \times 10^9 M_{\odot}$  black hole is able match the observed CO(1-0) kinematics.

Resolving the uncertainties in the NGC 1277 black hole mass requires high angular resolution observations that probe well within the region where the potential from the black hole dominates (the black hole sphere of influence,  $GM_{\text{BH}}/\sigma_*^2$ ). Here we present new IFU observations from the 8m Gem-

ini North telescope assisted by laser guide star adaptive optics (AO) and use orbit-based stellar dynamical models to revisit the black hole mass measurement of NGC 1277. In Section 2, we review the luminous mass model adopted for NGC 1277. We describe the AO spectroscopic observations in Section 3, the measurement of the high-angular resolution stellar kinematics in Section 4, and the corresponding PSF model in Section 5. Although the kinematics measured from the AO observations are used to constrain  $M_{\text{BH}}$  in our final model, we also run models that simultaneously fit to large-scale kinematics extending to several galaxy effective radii. These large-scale kinematics are discussed in Section 6. We describe the dynamical models in Section 7 and the results are given in Section 8. A discussion of the revised  $M_{\text{BH}}$  in comparison to past work and implications from the location of NGC 1277 on the black hole-galaxy relations is provided in Section 9, followed by concluding remarks in Section 10.

Throughout the paper, we assume a distance of 71 Mpc, which is the Hubble flow distance from the Virgo + Great Attractor + Shapley Supercluster Infall model (Mould et al. 2000) for  $H_0 = 70.5 \text{ km s}^{-1} \text{ Mpc}^{-1}$ ,  $\Omega_M = 0.27$  and  $\Omega_{\Lambda} = 0.73$ . At this distance,  $1''$  corresponds to 0.34 kpc. We further adopt  $R_e = 3''.5$  (1.2 kpc; Yildirim et al. 2015) and  $\sigma_* = 333 \text{ km s}^{-1}$  (van den Bosch et al. 2012; Kormendy & Ho 2013), which is also in agreement with the effective stellar velocity dispersion from large-scale IFU observations reported by Yildirim et al. (2015). For the galaxy's bulge luminosity, we apply bulge-to-total ( $B/T$ ) ratios determined through photometric bulge-disk decompositions of a *Hubble Space Telescope* (HST) V-band image to the 2MASS  $K_s$  total luminosity (Jarrett et al. 2000). However, we note that a dynamical decomposition derived from the best-fit model of Yildirim et al. (2015) shows a rotating central round component, in addition to several other strongly rotating elements, making NGC 1277's dynamical structure fundamentally different from BCGs and complicating the identification of a bulge. Therefore, NGC 1277's bulge luminosity is uncertain and we conservatively use  $L_{\text{bul}} = (7.7^{+2.8}_{-4.3}) \times 10^{10} L_{\odot}$  in the  $K$ -band, which comes from a bulge-to-total ratio of 0.55 (Kormendy & Ho 2013). The bounds on the bulge luminosity are taken from the photometric decomposition of Yildirim et al. (2015), who find lower and upper limits of  $B/T = 0.24$  and  $B/T = 0.75$ . This is also consistent with a  $B/T = 0.27$  measured by van den Bosch et al. (2012).

## 2. LUMINOUS MASS MODEL

We used the two-dimensional (2D) light distribution presented in van den Bosch et al. (2012), which was constructed from an archival HST Advanced Camera for Surveys (ACS) image. The ACS data were originally acquired under program GO-10546 with the F550M filter. The observations have a total integration time of 2439 s, and a spatial scale of  $0''.05 \text{ pixel}^{-1}$ . The light distribution is described using the Multi-Gaussian Expansion (MGE) method (Monnet et al. 1992; Emsellem et al. 1994), as such a representation can be analytically deprojected to determine the galaxy's intrinsic luminosity density. van den Bosch et al. (2012) generated the NGC 1277 MGE using Galfit (Peng et al. 2010) while accounting for a Tiny Tim PSF model (Krist & Hook 2004) that was dithered in the same manner as the galaxy observations. The elliptical galaxy NGC 1278, located  $47''$  away in projection, was simultaneously fit with NGC 1277, however other sources, including a nuclear dust disk, were masked and excluded from the fit. The dust disk has an apparent axis ratio of

0.3, suggesting that the galaxy is viewed near edge-on, with an inclination angle of  $75^\circ$ . As presented in Supplemental Table 1 of van den Bosch et al. (2012), the NGC 1277 MGE consists of 10 components, each with the same center and position angle of  $92.7^\circ$ . The dispersion of the Gaussians along the major axis extends from  $0''.06$  to  $17''$ , and the apparent flattening ranges between 0.4–0.9.

### 3. AO NIFS OBSERVATIONS

We obtained high angular resolution spectroscopy of NGC 1277 using the Near-infrared Integral Field Spectrometer (NIFS; McGregor et al. 2003) with the ALTitude conjugate Adaptive optics for the InfraRed (Herriot et al. 2000; Boccas et al. 2006) system on the Gemini North telescope. The observations were taken as part of program GN-2011B-Q-27 over the course of four nights, spanning from 2012 Oct 30 to 2012 Dec 27. We observed NGC 1277 using 600 s Object-Sky-Object exposures with the  $H+K$  filter and  $K$  grating centered on  $2.2 \mu\text{m}$ . For the galaxy observations we used the “open-loop” focus model (Krajnović et al. 2009) and the bright, compact nucleus as the tip-tilt star. We further acquired NIFS observations of a nearby star to measure the point spread function (PSF) and A0 V stars for telluric correction.

We reduced the NIFS data using IRAF tasks<sup>1</sup> in the Gemini/NIFS package version 1.11. The reduction followed the procedure outlined in the NIFS example processing scripts<sup>2</sup>. The main steps included sky subtraction, flat fielding, bad pixel and cosmic-ray cleaning, spectral and spatial rectification, telluric correction, and the creation of a data cube. Individual data cubes of the galaxy were summed along the wavelength axis to generate flux maps, which were then cross-correlated in order to determine the relative spatial offsets between cubes. Twelve galaxy exposures, totaling 2 hours-on source, were aligned and combined to produce the final data cube composed of a spectral dimension and  $x$  and  $y$  spatial dimensions with a scale of  $0''.05 \text{ pixel}^{-1}$ . The PSF observations were reduced in a similar manner.

We also retrieved NIFS  $K$ -band observations of K and M giant/supergiant stars, and the supporting calibration files, from the Gemini Science Archive. The twelve stars were originally observed under programs GN-2006A-C-11, GN-2006B-Q-107, GN-2007A-Q-62, and GN-2010A-Q-112. We followed the NIFS data reduction steps described above, but additionally extracted a one-dimensional spectrum for each star. We then rebinned the template spectra to the same wavelength range and sampling, and shifted the stars to rest. Nearly all of the stars are part of the NIFS Spectral Template Library v2.0<sup>3</sup> (Winge et al. 2009), however we chose to reduce the observations from scratch so that our template spectra would have a similar continuum shape as the observed galaxy spectra. Currently, the spectra associated with the NIFS Spectral Template Library have been continuum-divided on a star-by-star basis.

### 4. HIGH ANGULAR RESOLUTION STELLAR KINEMATICS

From the NIFS data cube, we extracted spectra over a range of spatial locations and used the Voronoi binning method (Cappellari & Copin 2003) to determine the optimal balance

between signal-to-noise (S/N) and bin size. We measured the line-of-sight velocity distribution (LOSVD) in each spatial bin using the penalized pixel fitting (pPXF) method (Cappellari & Emsellem 2004), parametrizing the LOSVD in terms of the radial velocity ( $V$ ), the velocity dispersion ( $\sigma$ ), and the next two Gauss-Hermite moments ( $h_3$ ,  $h_4$ ) that correspond to asymmetric and symmetric deviations from a Gaussian. An optimal stellar template in each spatial bin was constructed from a library of twelve stars observed with NIFS. The library includes K0–M5 giant stars, a K5 supergiant, and an M0 supergiant. Slight differences in the continuum shape and the equivalent width between the LOSVD-broadened optimal template and the observed galaxy spectrum were corrected for using an additive constant and a first degree multiplicative Legendre polynomial.

We fit between observed wavelengths of  $2.253\text{--}2.377 \mu\text{m}$ , and measured the kinematics primarily from the  $(2-0)^{12}\text{CO}$  and  $(3-1)^{12}\text{CO}$  stellar features. We chose this particular wavelength range to avoid artifacts in the outer spatial bins near the  $(4-2)^{12}\text{CO}$  bandhead and to avoid the Na I absorption line, as we were unable to achieve satisfactory fits due to the lack of dwarf stars in our template library (Krajnović et al. 2009; Walsh et al. 2012). For the same reason, we excluded the Ca I feature contained within our fitting region. We further excluded an artifact near the  $(3-1)^{12}\text{CO}$  bandhead.

Using the results of an initial fit to the observed galaxy spectrum in each spatial bin, we ran Monte Carlo simulations with 100 realizations. During each realization, we added random Gaussian noise to the best-fit model, such that the level of the perturbation is given by the standard deviation of model residuals. We set the pPXF penalization to zero to produce realistic uncertainties. From the resulting distribution for each Gauss-Hermite moment in each of the spatial bins, we calculated the mean and standard deviation, which we took to be the kinematic value and  $1\sigma$  uncertainty.

We tested the robustness of the NIFS kinematics by modifying the details of how the kinematics were extracted. Nearly all spatial bins have kinematics consistent at the  $1\sigma$  level (all are consistent within  $2\sigma$ ) with those measured using various combinations of degree 0–1 additive/multiplicative polynomials, as well as simply a multiplicative order 1 polynomial. Similar kinematics are also measured when including the Ca I feature, and when fitting over a longer wavelength region that extends to  $2.415 \mu\text{m}$  and includes the third major CO bandhead. Moreover, we tested keeping the relative mix of stars making up the optimal template fixed between spatial bins, but allowing the coefficients of the additive and multiplicative polynomial to vary. This produced consistent results as our default method of fitting for the optimal stellar template in each spatial bin.

As a final step, we point-symmetrize the NIFS kinematics using the procedure in van den Bosch & de Zeeuw (2010). We find that galaxy is rotating with velocities of  $\pm 350 \text{ km s}^{-1}$ . The velocity dispersion increases sharply to  $551 \text{ km s}^{-1}$  at the center from values of  $\sim 275 \text{ km s}^{-1}$  in the outer NIFS spatial bins. As is expected for an axisymmetric system, we find an anti-correlation between the  $h_3$  and  $V$  maps. We also observe a slight peak in  $h_4$  at the nucleus to values of  $\sim 0.05$ . The median error for  $V$ ,  $\sigma$ ,  $h_3$ , and  $h_4$  over the 105 spatial bins is  $7 \text{ km s}^{-1}$ ,  $9 \text{ km s}^{-1}$ ,  $0.02$ , and  $0.02$ , respectively. Taking the S/N to be the median flux divided by the standard deviation of model residuals from the initial fits with pPXF, we find S/N values of 69–164, with a median value of 92. Examples of the spectral

<sup>1</sup> IRAF is distributed by the National Optical Astronomy Observatory, which is operated by the Association of Universities for Research in Astronomy under cooperative agreement with the National Science Foundation

<sup>2</sup> <http://www.gemini.edu/sciops/instruments/nifs/data-format-and-reduction>

<sup>3</sup> <http://www.gemini.edu/sciops/instruments/nearir-resources/spectral-templates>

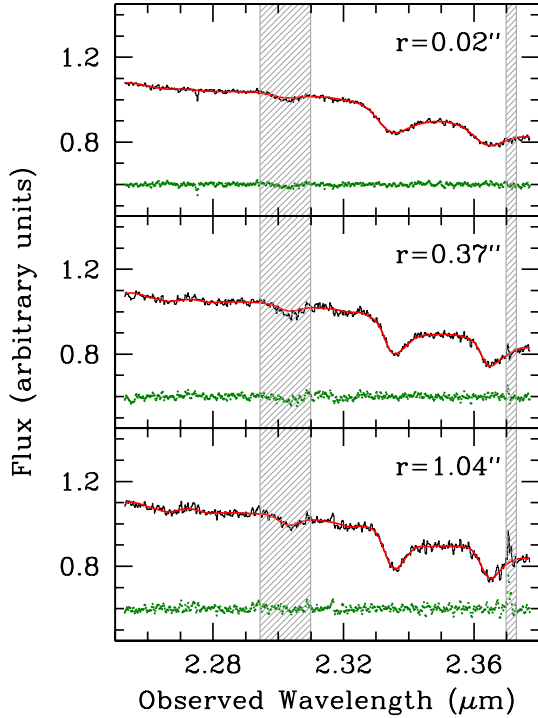


FIG. 1.— Example fits to the NIFS *K*-band CO bandheads at the nucleus (top), at an intermediate distance from the galaxy center (middle), and in one of the outermost spatial bins (bottom). The best-fit stellar template broadened by the LOSVD is plotted in red, and the model residuals, after adding an arbitrary constant, are displayed in green. Gray shaded boxes indicate the wavelength regions excluded from the fit.

fitting at three spatial locations are shown in Figure 1, and the kinematics prior to symmetrization are given in Table 1.

### 5. NIFS PSF MEASUREMENT

We modeled the NIFS PSF as the sum of two concentric, circular 2D Gaussians. The weights and dispersions of the components were determined by comparing the galaxy data cube, after summing along the wavelength axis, to the MGE model of the *HST* image convolved with the NIFS PSF model. The comparison was also used to determine the center of the NIFS aperture. The NIFS PSF was best described by an inner Gaussian with a dispersion of  $0''.07$  and a relative weight of 0.65 and an outer Gaussian with a dispersion of  $0''.40$  and a weight of 0.35. Using more than two Gaussians to model the PSF produced components with negligible weights.

Since the NIFS PSF is a vital input into the dynamical models when measuring  $M_{\text{BH}}$ , we also estimated the PSF by examining NIFS observations of a nearby star. Using Galfit, we found that the sum of four concentric, circular Gaussians provided a good description of the collapsed data cube. The best-fit model was composed of Gaussians weighted by 0.14, 0.31, 0.34, and 0.20 with dispersions of  $0''.04$ ,  $0''.08$ ,  $0''.29$ , and  $0''.72$ , respectively. Therefore, we recover a similar NIFS PSF model using this alternative method, and both NIFS PSFs are typical of the Gemini AO system (e.g., Krajnović et al. 2009; Gebhardt et al. 2011; Onken et al. 2014; Seth et al. 2014). Although we utilize the two Gaussian PSF model described above for the final dynamical models, in Section 8 we also test the effect on  $M_{\text{BH}}$  of adopting the four-component model estimated from the NIFS PSF star observations.

### 6. LARGE-SCALE SPECTROSCOPY

The NIFS kinematics are the primary data used to constrain the NGC 1277 black hole mass in Section 8. However, we also tested running models that include large-scale stellar kinematics measured from HET Low Resolution Spectrograph (LRS; Hill et al. 1998) data and spectroscopy obtained at the 3.5m telescope at Calar Alto Observatory using the Potsdam Multi Aperture Spectrograph (PMAS; Roth et al. 2005) in the Pmas fiber PAcK (PPAK; Verheijen et al. 2004; Kelz et al. 2006) mode. The HET and PPAK observations, stellar kinematics (measured out to  $\sim 3 R_e$ ), and PSF models have been previously presented by van den Bosch et al. (2012) and Yildirim et al. (2015). Although we refer the reader to these publications for additional details, we briefly review the relevant information below.

The HET observations were taken with a  $1''$ -wide slit, the *g*2 grating, and  $2 \times 2$  binning, which provides an instrumental dispersion of  $108 \text{ km s}^{-1}$  and a wavelength coverage of  $4200 - 7400 \text{ \AA}$ . A single 900 s exposure was obtained along the galaxy major axis. After constructing 31 spatial bins, the stellar kinematics were measured with pPXF using the MILES template library (Sánchez-Blázquez et al. 2006; Falcón-Barroso et al. 2011) and a degree 25 multiplicative polynomial and an order 5 additive polynomial. By comparing the reconstructed slit image to the NGC 1277 MGE model and parameterizing the PSF as the sum of two Gaussians, weights of 0.66 and 0.34 and dispersions of  $0''.62$  and  $2''.80$ , respectively, were measured.

For the PPAK observations, two 900 s science exposures at three pointings (totaling 1.5 hours on-source) were acquired using the medium-resolution V1200 grating. With this setup, the useful spectral range is  $3650 - 4620 \text{ \AA}$  and the spectral resolution corresponds to  $R \sim 1650$  at  $4000 \text{ \AA}$ . The PPAK kinematic measurements for NGC 1277 were made within 38 Voronoi spatial bins using pPXF, with an additive degree 15 Legendre polynomial, and the Indo-U.S. Library of Coudé Feed Stellar Spectra (Valdes et al. 2004). The PPAK PSF is described by the sum of two Gaussians with dispersions of  $1''.21$  and  $2''.44$  with weights of 0.75 and 0.25, respectively. Thus, the PPAK data have a lower spatial resolution than the HET observations.

### 7. DYNAMICAL MODELS

We constrained the mass distribution of NGC 1277 using the three-integral, triaxial, orbit-based models from van den Bosch et al. (2008). The black hole mass recovery of the code was previously tested by van den Bosch & de Zeeuw (2010). With this method, the galaxy's gravitational potential is constructed from the combination of the black hole, the stars, and a Navarro-Frenk-White (NFW; Navarro et al. 1996) dark matter halo. The intrinsic stellar mass distribution is found by deprojecting the surface brightness model in Section 2 assuming an oblate axisymmetric shape, an inclination angle of  $75^\circ$ , and a V-band stellar mass-to-light ratio ( $\Upsilon_V$ ) that remains constant with radius. NGC 1277 appears very flattened, is a fast rotator, and doesn't show signs of kinematic twists – all of which support the assumption of axisymmetry. The inclination angle is the same as the one assumed in previous studies of NGC 1277 (van den Bosch et al. 2008; Emsellem 2013; Yildirim et al. 2015), and is set by the nuclear dust disk in the optical *HST* image. In our models, the NFW halo is described by the concentration parameter ( $c$ ), which we set to 10, and the fraction of dark matter relative to the stellar mass ( $f_{\text{DM}}$ ), which we set to values of 10, 100, and

TABLE 1  
NIFS KINEMATICS

$x$ (") (1)	$y$ (") (2)	$V$ (km s <sup>-1</sup> ) (3)	$\Delta V$ (km s <sup>-1</sup> ) (4)	$\sigma$ (km s <sup>-1</sup> ) (5)	$\Delta\sigma$ (km s <sup>-1</sup> ) (6)	$h_3$ (7)	$\Delta h_3$ (8)	$h_4$ (9)	$\Delta h_4$ (10)
0.004	-0.021	-8.361	9.999	579.913	15.292	-0.015	0.011	0.055	0.015
0.004	0.029	-21.369	7.795	522.633	11.262	-0.007	0.012	0.037	0.015
-0.046	-0.021	122.570	6.853	518.453	9.756	-0.035	0.010	0.061	0.013
-0.046	0.029	98.918	6.632	469.906	7.982	-0.030	0.013	0.039	0.014
0.054	-0.021	-44.814	7.965	575.108	17.143	0.007	0.011	0.061	0.016

NOTE. — The Voronoi bin  $x$  and  $y$  generators are given in Columns (1) and (2), and the NIFS unsymmetrized kinematics and errors are presented in Columns (3)-(10). The position angle is 177.24° counterclockwise from the galaxy's major axis to  $x$ . This table is available in its entirety in machine-readable form.

1000, corresponding to halo virial masses of  $\sim 10^{12}$ ,  $\sim 10^{13}$ , and  $\sim 10^{14} M_\odot$ . We also ran models that do not incorporate a dark halo. For  $M_{\text{BH}}$  and  $\Upsilon_{\text{V}}$ , we sampled 31 values between  $5 \times 10^8$  and  $5 \times 10^{10} M_\odot$  and 41 values from 5.0–15.0  $\Upsilon_\odot$ , respectively.

For a given galaxy potential set by  $M_{\text{BH}}$ ,  $\Upsilon_{\text{V}}$ ,  $c$ , and  $f_{\text{DM}}$ , we generated an orbit library that samples 32 logarithmically spaced equipotential shells at radii from 0''003 to 85'', starting at 9 angular and 9 radial values at each energy. We further bundle together 125 orbits with adjacent initial conditions to ensure a smooth distribution function, yielding a total of 972,000 orbits. The orbits are integrated in the potential, and after accounting for the PSF and aperture binning, weights are assigned to the orbits through a non-negative least squares process such that their combined properties match the intrinsic and projected stellar masses along with the observed kinematics. We required that the surface brightness and three-dimensional mass distributions be fit to an accuracy of 1%. Since we are most interested in the mass of the black hole in NGC 1277, we reduce the effects on  $M_{\text{BH}}$  associated with our choices of dark halo parameterization and a constant mass-to-light ratio by fitting to only the NIFS kinematics. With four Gauss-Hermite moments measured in 105 NIFS spatial bins, there are 420 observables.

## 8. RESULTS

When fitting stellar-dynamical models to the point-symmetrized NIFS kinematics, we find that  $M_{\text{BH}}$  is well constrained, as can be seen in Figure 2. We measured the formal  $1\sigma$  and  $3\sigma$  modeling fitting uncertainties by examining the  $\chi^2$  after marginalizing over the other three parameters and searching for where the  $\chi^2$  has increased by 1 and 9, respectively, from the minimum ( $\chi^2_{\text{min}}$ ). This corresponds to  $M_{\text{BH}} = (4.9 \pm 0.2) \times 10^9 M_\odot$  and  $\Upsilon_{\text{V}} = 9.3 \pm 0.4 \Upsilon_\odot$  ( $1\sigma$ ), and  $M_{\text{BH}} = (4.9^{+1.2}_{-1.4}) \times 10^9 M_\odot$  and  $\Upsilon_{\text{V}} = 9.3^{+2.1}_{-1.9} \Upsilon_\odot$  ( $3\sigma$ ). As expected, the dark halo cannot be constrained with the NIFS data; all three dark halos and the model without dark matter are within  $\Delta\chi^2 \equiv \chi^2 - \chi^2_{\text{min}} = 5$ . The best-fit model is compared to the observed NIFS kinematics in Figure 3 and Figure 4, and is an excellent match to the data with a reduced  $\chi^2$  of 0.7. The best-fit model is able to reproduce the dramatic rise in the stellar velocity dispersion at the nucleus and the slight increase in  $h_4$  at the center.

We further tested the robustness of the  $M_{\text{BH}}$  and  $\Upsilon_{\text{V}}$  results by examining the change in the best-fit values when assuming a different PSF, when using unsymmetrized kinematics, and when adopting a different pPXF continuum-correction model while extracting the NIFS kinematics. Given the challenges associated with the PSF measurement due to the evolving AO correction and the merging of data cubes that span sev-

eral nights, it is important to test how other reasonable PSF parameterizations affect  $M_{\text{BH}}$ . For the fiducial model presented above, we utilized a two-Gaussian PSF model measured from the comparison of the MGE to the NGC 1277 collapsed NIFS data cube. As a secondary approach, we test using the sum of four Gaussians to describe the PSF, which was determined from NIFS PSF star observations. In comparison to the two-Gaussian PSF model, the core of the four-Gaussian PSF model has a similar dispersion but a lower weight, such that the core makes up 45% of the total flux. Using this four-Gaussian PSF model results in the best-fit  $M_{\text{BH}}$  increasing by 22% to  $6.0 \times 10^9 M_\odot$  and  $\Upsilon_{\text{V}}$  decreasing by 14% to 8.0  $\Upsilon_\odot$ .

The next test we ran involved fitting stellar-dynamical models to the unsymmetrized NIFS kinematics. Symmetrization is commonly used to reduce noise in the observed kinematic measurements. Our fiducial model was fit to NIFS kinematics that were averaged in a two-fold symmetric way about the major and minor axes while accounting for the flux each spaxel contributed to the spatial bin and the kinematic error of the bin. If instead no adjustments are made to the observed NIFS kinematics, with the exception of subtracting off the offsets in the odd Gauss-Hermite moments (e.g., the galaxy's recessional velocity), then we measure a black hole mass of  $5.8 \times 10^9 M_\odot$  and a V-band stellar mass-to-light ratio of 8.8  $\Upsilon_\odot$ . Hence,  $M_{\text{BH}}$  increases by 18% and  $\Upsilon_{\text{V}}$  decreases by 5%. The best-fit model to the unsymmetrized NIFS kinematics has a reduced  $\chi^2$  of 2.9.

Finally, the NIFS kinematics appear to be sensitive to the adopted pPXF continuum-correction model. We measured the stellar kinematics by comparing spectra of K and M giant and supergiant stars to the NGC 1277 spectra. Since the stars were also observed with NIFS, their spectra have a similar shape as the galaxy spectra; however, minor adjustments to the templates are needed to account for differences in the CO bandhead equivalent widths and for reddening/imperfect flux calibration. In order to provide a better match to the observed galaxy spectra, we used additive/multiplicative Legendre polynomials with pPXF. As described in Section 4, we selected an additive degree 0 and multiplicative degree 1 polynomial, and allowed pPXF to solve for the best-fit coefficients simultaneously with the Gauss-Hermite moments. An additive degree 0 and multiplicative degree 1 polynomial produced a good fit to the NGC 1277 observations, and the use of other low-order polynomials yield consistent kinematics.

Adopting higher-order polynomials resulted in slightly better fits to the galaxy spectra, but generally lower stellar velocity dispersions, especially at the nucleus. Notably, extracting the NIFS kinematics using a multiplicative degree 2 polynomial resulted in velocity dispersions that were lower by as much as 36 km s<sup>-1</sup> compared to when an additive de-

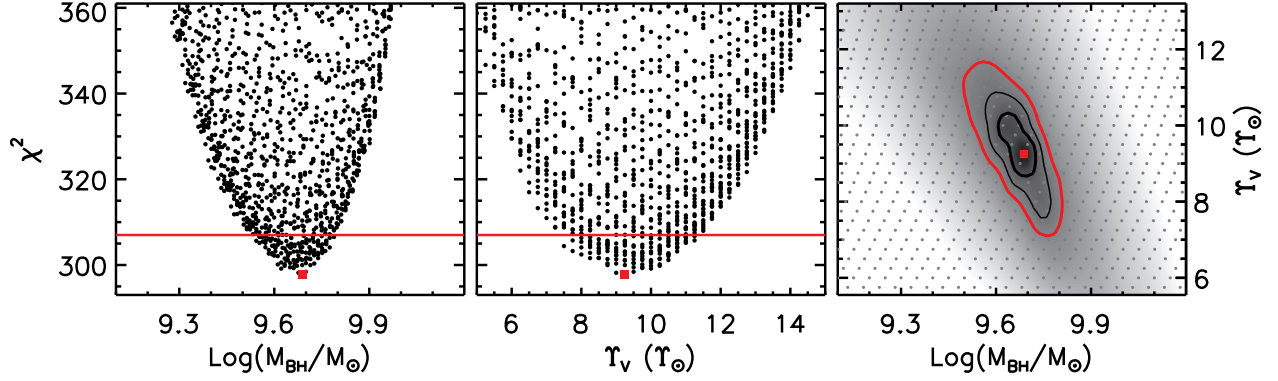


FIG. 2.— Results of stellar-dynamical models fit to the NIFS kinematics. The  $\chi^2$  is shown with black hole mass (left panel) and  $V$ -band mass-to-light ratio (middle panel). Each black dot corresponds to a single model, with the best-fit model highlighted as the red square. The red solid line indicates where  $\Delta\chi^2 = 9.0$ , corresponding to the  $3\sigma$  confidence level for one parameter.  $\chi^2$  contours are shown for a grid of black hole masses and mass-to-light ratios (right panel). Each gray point represents a model, and the best-fit model (red square) corresponds to  $M_{\text{BH}} = 4.9 \times 10^9 M_\odot$  and  $\Upsilon_V = 9.3 \Upsilon_\odot$ . Relative to the minimum, the  $\chi^2$  has increased by 2.3 (thick black contour), 6.2 (thin black contour), and 11.8 (red contour), corresponding to the  $1\sigma$ ,  $2\sigma$ , and  $3\sigma$  confidence intervals for two parameters.

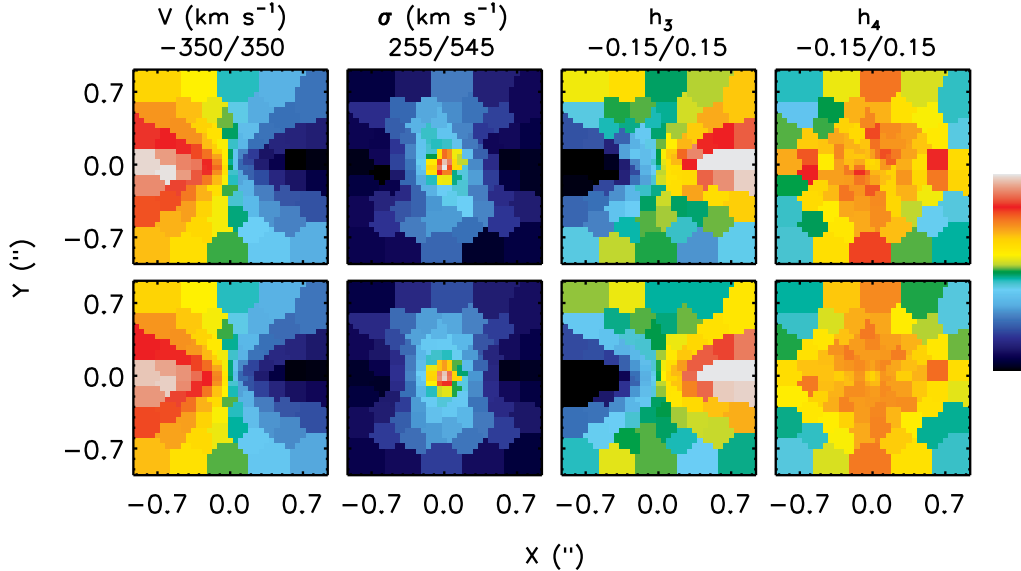


FIG. 3.— The observed NIFS kinematics (top) show that NGC 1277 is rotating, with the west side of the galaxy being blue-shifted, that there is a sharp rise in the velocity dispersion and generally positive  $h_4$  values at the nucleus, and that  $h_3$  and  $V$  are anti-correlated. The best-fit stellar dynamical model (bottom) is shown on the same scale given by the color bar to the right and the minimum/maximum values are provided at the top of the maps. The best-fit model nicely reproduces the NIFS observations and has a reduced  $\chi^2$  of 0.7.

gree 0 with a multiplicative degree 1 polynomial were utilized. Other combinations of multiplicative degree 2–4 polynomials with no additive contribution, or with additive degree 0–1 polynomials, produced consistent kinematics as the multiplicative degree 2 polynomial case. Therefore, we tested the effect on  $M_{\text{BH}}$  when fitting to point-symmetrized NIFS kinematics extracted with an order 2 multiplicative polynomial. We found that the black hole mass decreased to  $4.2 \times 10^9 M_\odot$ , or by 14%, and the  $V$ -band stellar mass-to-light ratio increased to  $10.0 \Upsilon_\odot$ , or by 8%.

The final uncertainties are determined by adding in quadrature the change in the  $M_{\text{BH}}$  and  $\Upsilon_V$  from each of the three tests above and the  $1\sigma$  statistical errors from the fiducial model grid. This results in fractional errors of 32% and 17% on  $M_{\text{BH}}$  and  $\Upsilon_V$ , respectively. In other words,  $M_{\text{BH}} = (4.9 \pm 1.6) \times$

$10^9 M_\odot$  and  $\Upsilon_V = 9.3 \pm 1.6 \Upsilon_\odot$ . The systematics associated with the NIFS kinematics and NIFS PSF input into the stellar-dynamical models dominate over the formal  $1\sigma$  model fitting uncertainty. In terms of other common systematic sources of error that plague stellar-dynamical measurements, by fitting to just the NIFS kinematics we have limited mass degeneracies with the galaxy’s dark halo (e.g., Gebhardt & Thomas 2009; Rusli et al. 2013) and uncertainties associated with the assumption of a constant stellar mass-to-light ratio (e.g., McConnell et al. 2013). Moreover, owing to the presence of the nuclear dust disk, uncertainty in the viewing orientation is minimal, unlike some past stellar-dynamical studies (e.g., Shapiro et al. 2006; Onken et al. 2007). The dust disk, however, may be problematic for construction of the luminous mass model in Section 2. We conservatively masked the dust



when generating the MGE model, but acknowledge that if the MGE under-predicts the nuclear stellar mass then the black hole mass would be overestimated.

### 8.1. Models with Large-scale Kinematics

Large-scale data is commonly used to complement high angular resolution spectroscopy in order to better constrain the stellar mass-to-light ratio and orbital distribution (e.g., Shapiro et al. 2006; Krajnović et al. 2009). The NIFS kinematics extend out to a radius of  $1''.3$  (442 pc), or  $\sim 0.4 R_e$ . Therefore, the NIFS data not only resolve the black hole sphere of influence, but also probe the region where the stars begin to dominate the potential. It is encouraging that our fiducial model presented at the beginning of Section 8 largely reproduces the observed HET kinematics over the radial range of the NIFS data, as can be seen in Figure 4. The predictions from this best-fit model, constrained by only the NIFS kinematics, are consistent with the velocity, velocity dispersion, and  $h_3$  HET measurements, and only deviate from the central  $h_4$  HET values by about 1.5 times the measurement uncertainty. Although the fiducial model is in fair agreement with the HET observations, Figure 4 shows that the same model is worse at matching the observed PPAK kinematics. The predictions from the best-fit model constrained only by the NIFS data are consistent with the velocity and  $h_3$  PPAK measurements, but over-estimate the central PPAK velocity dispersions by about nine times the measurement errors, in addition to under-predicting the inner  $h_4$  PPAK values by twice the uncertainty.

Therefore, we also ran dynamical models that fit to the combination of NIFS and HET kinematics, as well as to the combination of NIFS and PPAK kinematics, continuing to sample the same dark halos described in Section 7. We recovered best-fit values of  $M_{\text{BH}} = 4.8 \times 10^9 M_\odot$  and  $\Upsilon_V = 10.3 \Upsilon_\odot$  with a reduced  $\chi^2$  of 0.8 when fitting all 31 HET spatial bins, and  $M_{\text{BH}} = 4.6 \times 10^9 M_\odot$  and  $\Upsilon_V = 9.8 \Upsilon_\odot$  with a reduced  $\chi^2$  of 0.8 when excluding three outer bins because their dispersions are below the HET/LRS instrumental resolution. Instead if dynamical models are fit to the combination of the NIFS and PPAK kinematics, we infer  $M_{\text{BH}} = 6.1 \times 10^9 M_\odot$  and  $\Upsilon_V = 8.3 \Upsilon_\odot$  with a reduced  $\chi^2$  of 0.8. In summary, we find that the black hole mass and mass-to-light ratio measured from models fit to NIFS+HET and NIFS+PPAK agree with the results from our fiducial model, fit to NIFS only, after accounting for systematics associated with the NIFS kinematics and PSF.

## 9. DISCUSSION

Below we compare our black hole mass measurement to the previous mass determinations in the literature and discuss the implications of NGC 1277's location on the black hole–host galaxy relations.

### 9.1. Comparison to Previous Black Hole Mass Measurements

With  $M_{\text{BH}} = 4.9 \times 10^9 M_\odot$  and  $\sigma_* = 333 \text{ km s}^{-1}$ , the NIFS observations probe well within the black hole sphere of influence of  $0''.6$ . Previous stellar-dynamical work using seeing-limited data from long-slit HET observations and IFU PPAK observations found  $M_{\text{BH}} = 1.7 \times 10^{10} M_\odot$  (van den Bosch et al. 2012) and  $M_{\text{BH}} = 1.2 \times 10^{10} M_\odot$  (Yildirim et al. 2015), respectively. Neither study, however, quantified the impact of possible systematic effects on the NGC 1277 black hole mass.

In particular, Emsellem (2013) found that the HET kinematics presented in van den Bosch et al. (2012) could be nearly reproduced with a  $5 \times 10^9 M_\odot$  black hole. A rather small deviation between the  $5 \times 10^9 M_\odot$  black hole model and the HET kinematics occurs for the innermost  $h_4$  measurements, such that the model under-predicts the observed values by about twice the uncertainty, which is similar to our best-fit model. Given the possibility of spurious kinematic measurements due to issues like template mismatch, Emsellem (2013) advocated for the use of  $3\sigma$  confidence levels for a more conservative estimate of the  $M_{\text{BH}}$  uncertainty. For stellar-dynamical models fit to the HET kinematics, the  $3\sigma$  uncertainty corresponds to  $M_{\text{BH}} = (6.5 - 32) \times 10^9 M_\odot$  and  $\Upsilon_V = 0.1 - 9.7 \Upsilon_\odot$  (van den Bosch et al. 2012).

Similarly, Yildirim et al. (2015) opted to report  $3\sigma$  statistical uncertainties as a careful way in which to assign errors to  $M_{\text{BH}}$  and  $\Upsilon_V$ . They fit to both PPAK and HET observations simultaneously to determine  $M_{\text{BH}} = (1.3^{+0.3}_{-0.5}) \times 10^{10} M_\odot$  and  $\Upsilon_V = 6.5 \pm 1.5 \Upsilon_\odot$ . They comment though that the central dispersion and  $h_4$  measurements from the PPAK data are systematically lower than the inner values from the HET data, which could be due to a number of reasons (e.g., the use of different stellar libraries, different spectral fitting regions, different spatial resolutions, etc.). Since the PPAK data provide an independent check of the validity of the HET kinematics, Yildirim et al. (2015) additionally fit orbit-based models to only the PPAK kinematics, finding a lower limit of  $M_{\text{BH}} = 4.0 \times 10^9 M_\odot$ , which they view as a very conservative bound on the NGC 1277 black hole mass.

Therefore, our black hole mass of  $(4.9 \pm 1.6) \times 10^9 M_\odot$  and V-band mass-to-light ratio of  $9.3 \pm 1.6 \Upsilon_\odot$  are in agreement with the above conservative limits from van den Bosch et al. (2012) and Yildirim et al. (2015). Although it is tempting to assume that the smaller black hole mass inferred from the NIFS data is the result of smaller central  $h_4$  values as suggested by Figure 4, much of the inferred black hole mass is being driven by the lower order moments, and not  $h_4$ . If dynamical models are fit to only the NIFS velocity, velocity dispersion, and  $h_3$  measurements, we recover a best-fit black hole mass consistent with  $M_{\text{BH}} = (4.9 \pm 1.6) \times 10^9 M_\odot$ . Similarly, if an artificial constant is added to the observed NIFS  $h_4$  values (we tested adding an offset of 0.03 and 0.06), no change in the black hole mass outside of the quoted uncertainties is observed.

A more rigorous comparison ultimately requires an attempt to quantify some possible systematics that affect  $M_{\text{BH}}$  and  $\Upsilon_V$  derived from the low spatial resolution data. For example, the HET and PPAK kinematics from van den Bosch et al. (2012) and Yildirim et al. (2015) extend to  $\sim 3 R_e$  ( $\sim 10''$ ), and both studies assumed that the stellar mass-to-light ratio remains constant over this radial range. Yildirim et al. (2015) argued against a varying mass-to-light ratio based on a lack of color gradients in Sloan Digital Sky Survey (SDSS) imaging, but Martín-Navarro et al. (2015) find a possible increase in  $\Upsilon_V$  from  $7.5 \Upsilon_\odot$  at  $\sim 5''$  to  $11.6 \Upsilon_\odot$  at  $\sim 1''$  by measuring gravity sensitive absorption lines in optical/near-infrared spectra of NGC 1277 and assuming a bimodal initial mass function. Since the large-scale HET and PPAK spectroscopy do not resolve the black hole sphere of influence, the assumptions made about the mass-to-light ratio will have a significant impact on  $M_{\text{BH}}$  (e.g., Rusli et al. 2013). If  $\Upsilon_V$  is actually larger at the center than that assumed by van den Bosch et al. (2012) and Yildirim et al. (2015), then their inferred  $M_{\text{BH}}$  is

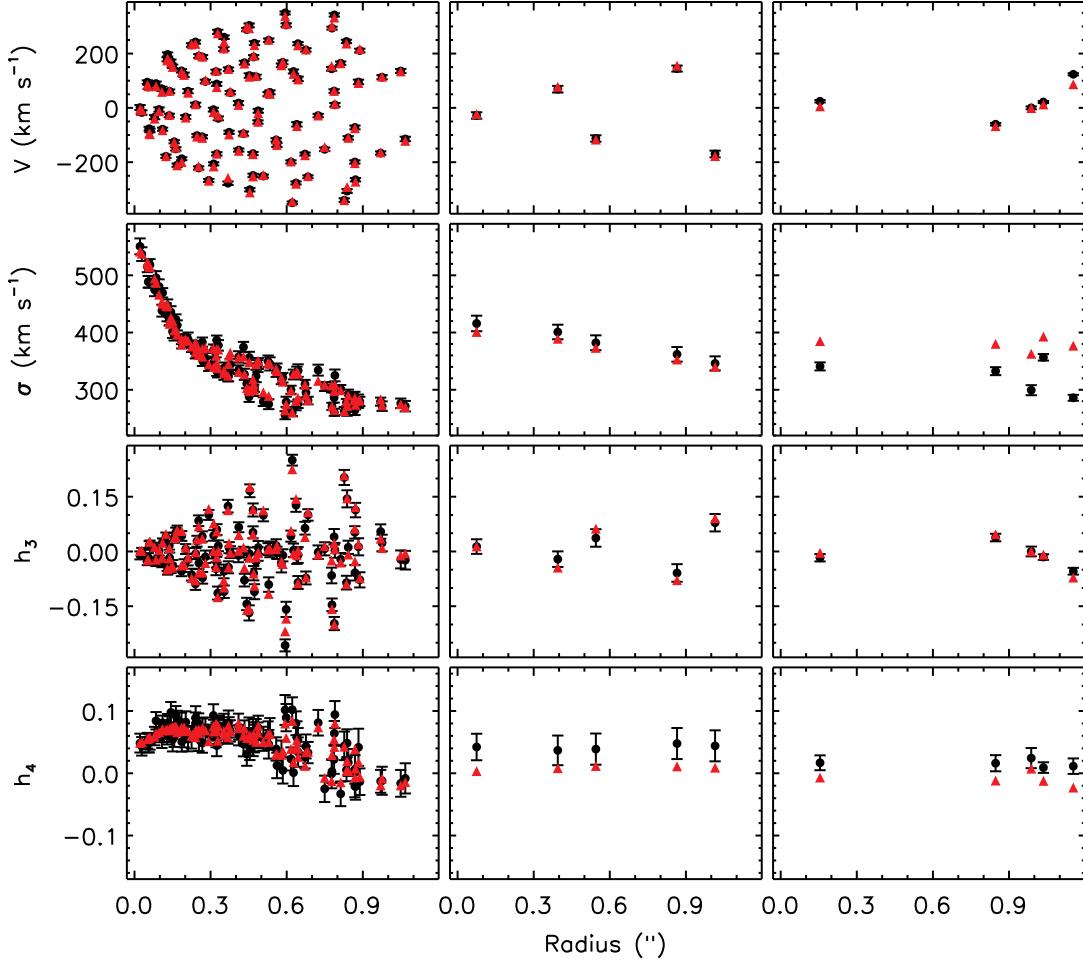


FIG. 4.— The observed kinematics (black circles) measured from NIFS (left column), HET (middle column), and PPAK (right column) are shown over the radial extent of the NIFS data. The data have been folded and are plotted as a function of projected distance from the nucleus. While the HET measurements have been made along the galaxy major axis, multiple position angles are depicted for the IFU data. For comparison, we plot the best-fit model constrained by only the NIFS kinematics (red triangles). Thus, the best-fit model predictions for the central HET and PPAK kinematics take into account differences in spatial resolution. The best-fit model generally reproduces the observed central HET kinematics but is a worse match to the observed innermost PPAK kinematics. Instead, fitting dynamical models to NIFS+HET and to NIFS+PPAK produces black hole masses and mass-to-light ratios that are consistent with  $M_{\text{BH}} = (4.9 \pm 1.6) \times 10^9 M_{\odot}$  and  $\Upsilon_V = 9.3 \pm 1.6 \Upsilon_{\odot}$ , found by fitting models to NIFS only.

overestimated.

The factor of  $\sim 3$  difference in the best-fit black hole masses between this work and the prior stellar-dynamical studies is large. However, incorporating any identifiable systematics into the error budget may make the  $M_{\text{BH}}$  and  $\Upsilon_V$  measurements from the AO spectroscopy and the large-scale spectroscopy come into better agreement than it currently appears based simply on the  $1\sigma$  model fitting uncertainties. We have done this in Section 8 for  $M_{\text{BH}}$  and  $\Upsilon_V$  derived from the AO observations; it is notable that the uncertainties associated with the extraction of the NIFS kinematics and the NIFS PSF alone dominate over the  $1\sigma$  statistical errors.

In addition to above stellar-dynamical black hole mass measurements, recently Scharwächter et al. (2015) presented cold molecular gas kinematics from low angular resolution radio observations of NGC 1277. Scharwächter et al. (2015) modeled the molecular gas distribution from the  $\sim 1''$  resolution and  $\sim 2''/5$  resolution configurations of PdBI as a nuclear ring and as an exponential disk with an inclination angle of  $75^\circ$ . Since the CO(1-0) emission was spatially unresolved, the black hole mass was not well constrained and they found

that the double-horned CO profile was consistent with both  $M_{\text{BH}} = 5 \times 10^9 M_{\odot}$  and  $M_{\text{BH}} = 1.7 \times 10^{10} M_{\odot}$ . Thus, the black hole mass measurement presented here is consistent with constraints from molecular gas kinematics, and it would be interesting to compare to higher angular resolution gas kinematics. Currently, there are a very limited number of meaningful comparisons between stellar and gas-dynamical black hole mass measurement methods (e.g., de Francesco et al. 2006; Neumayer et al. 2007; Cappellari et al. 2009; Gebhardt et al. 2011; Walsh et al. 2012, 2013).

## 9.2. NGC 1277 on the Black Hole Scaling Relations

The smaller inferred black hole mass from this work does not change the main result that NGC 1277 harbors an over-massive black hole for the galaxy’s luminosity, although NGC 1277 is now more consistent with the  $M_{\text{BH}} - \sigma_*$  relation. In Figure 5, we plot NGC 1277 on the black hole-galaxy relations. The black hole mass expected from  $M_{\text{BH}} - L_{\text{bul}}$  is  $(1.5 - 6.1) \times 10^8 M_{\odot}$  for  $K$ -band bulge luminosities between  $(3.4 - 11.0) \times 10^{10} L_{\odot}$  (Kormendy & Ho 2013), while the mass expected from  $M_{\text{BH}} - \sigma_*$  is  $(2.9 - 3.7) \times 10^9 M_{\odot}$  depending



on whether the McConnell & Ma (2013) or Kormendy & Ho (2013) calibration is used. Therefore, NGC 1277 is an order of magnitude above the mass expected from the  $M_{\text{BH}} - L_{\text{bul}}$  relation. The model with a  $8.1 \times 10^8 M_{\odot}$  black hole, which is the mass expected from  $M_{\text{BH}} - L_{\text{bul}}$  when conservatively using the galaxy’s total luminosity, is clearly a poor match to the NIFS observations and under-predicts the strong rise in the nuclear velocity dispersion and the minor increase in central  $h_4$  values, as can be seen in Figure 6. In contrast, the model with a larger black hole of  $M_{\text{BH}} = 1.7 \times 10^{10} M_{\odot}$ , which is the best-fit mass from van den Bosch et al. (2012), clearly overestimates the NIFS central velocity dispersion and  $h_4$  values.

NGC 1277 is similar to the galaxies highlighted in Kormendy & Ho (2013) as “black hole monsters”, namely NGC 4486B, NGC 4342, and NGC 1332, as well as the recently studied galaxies M60-UCD1 and NGC 1271. In particular, NGC 4342, NGC 1332, and NGC 1271 appear most like NGC 1277. All of these early-type galaxies are small, are outliers from the Faber-Jackson relation (i.e., show high velocity dispersions for their luminosities), are rotating, and are positively offset from  $M_{\text{BH}} - L_{\text{bul}}$  but consistent with  $M_{\text{BH}} - \sigma_*$ . Although less certain, there are hints that the galaxies Mrk 1216 (Yildirim et al. 2015) and SDSS J151741.75-004217.6 (Läsker et al. 2013) are also offset from  $M_{\text{BH}} - L_{\text{bul}}$ . We note that this behavior could differ from that observed for BCGs, as new measurements (McConnell et al. 2012) may indicate that the  $M_{\text{BH}} - \sigma_*$  relationship saturates, such that  $M_{\text{BH}}$  becomes independent of  $\sigma_*$  at large masses, but that BCGs continue to follow  $M_{\text{BH}} - L_{\text{bul}}$  (McConnell & Ma 2013; Kormendy & Ho 2013). If compact, high-dispersion galaxies like NGC 1277 and BCGs indeed exhibit different scaling relations, that would suggest that the black holes/galaxies grew via different pathways.

There are a few potential explanations for the presence of these over-massive black holes. One interesting possibility is that the galaxies are relics of the  $z \sim 2$  quiescent galaxies, passively evolving since that epoch. Ferré-Mateu et al. (2015) argue this is the case for NGC 1277 and NGC 1271, citing uniform old stellar populations (ages  $\gtrsim 10$  Gyr) and small sizes that make the galaxies outliers from the local mass-size relation of Shen et al. (2003). An equivalent picture was previously discussed by Trujillo et al. (2014), who also find uniform old stellar ages for NGC 1277, make note of the galaxy’s massive and compact nature, and point to an identical stellar mass density to the massive, high- $z$  passive galaxies as another indication that NGC 1277 is a relic galaxy. In particular, Ferré-Mateu et al. (2015) and Trujillo et al. (2014) suggest that the compact galaxies took a different evolutionary path than the one assumed for local massive galaxies, skipping a phase in which galaxies grow in size and mildly in mass via mergers after  $z \sim 2$ . Most recently, Wellons et al. (2015) echoed an analogous sentiment based on the analysis of Illustris simulations. Likewise, Fabian et al. (2013) proposed that a majority of black hole growth occurred before  $z \sim 3$  and that the accretion of gas and stars dictates whether there is subsequent evolution of the compact bulges. In other words, maybe galaxies like NGC 1277 are positive outliers from the local  $M_{\text{BH}} - L_{\text{bul}}$  relation because they reflect a previous time when galaxies harbored over-massive black holes, and the growth of host galaxies had yet to catch up.

A second explanation for the over-massive black holes is that these objects are simply unusual, and are found in the tails of a distribution between black hole masses and host galaxy

properties. With the limited number of dynamical measurements for  $\gtrsim 10^9 M_{\odot}$  black holes currently available, the form and scatter of the relations in this high-mass regime are not well established (McConnell & Ma 2013). Therefore, it is difficult to assess how much these compact, high-dispersion galaxies in reality deviate from the local  $M_{\text{BH}} - L_{\text{bul}}$  relation. Another way in which to create an over-massive black hole is through tidal stripping. This is believed to be the case for M60-UCD1 (Seth et al. 2014), however NGC 1277 does not show signs of recent interactions and the isophotes from the *HST* image appear regular without asymmetries. Another idea was put forth by Shields & Bonning (2013), who examine the possibility that the black hole was ejected from the BCG of Perseus, wandered about the cluster core, and was subsequently captured by NGC 1277. This, however, requires a series of rare events, and the scenario has become more unlikely as we now have confirmed another over-massive black hole (Walsh et al. 2015) and have a number of other candidates (van den Bosch et al. 2012, 2015; Ferré-Mateu et al. 2015) from galaxies also located in the Perseus cluster.

More dynamical mass measurements of the black holes in galaxies like NGC 1277 are needed, especially if such objects turn out to be the relics of higher redshift quiescent galaxies. Roughly 1 in 100 of the  $z \sim 2$  passive galaxies survive until today (Trujillo et al. 2009; van der Wel et al. 2014; Saulder et al. 2015). Although such relics are thought to be rare and are not representative of the local galaxy population, dynamically measuring  $M_{\text{BH}}$  in a significant sample will provide insight into the growth of black holes with their host galaxies over time. The HET Massive Galaxy Survey (van den Bosch et al. 2015) has uncovered about a dozen galaxies with sizes, dispersions, and luminosities similar to NGC 1277. We currently have high angular resolution imaging and spectroscopy for half of these objects, and are working on acquiring secure  $M_{\text{BH}}$  measurements.

## 10. CONCLUSION

We have presented *K*-band spectroscopic observations of the nearby S0 galaxy NGC 1277 obtained with Gemini/NIFS assisted by AO. The observations allow us to map out the stellar kinematics well with the black hole’s gravitational sphere of influence, and when combined with high resolution *HST* imaging, we are able to place strong constraints on the mass of the central black hole. We find that  $M_{\text{BH}} = (4.9 \pm 1.6) \times 10^9 M_{\odot}$ . These error bars reflect the  $1\sigma$  statistical uncertainties in combination with systematics associated with the NIFS kinematic measurements and the PSF model. We elect to fit orbit-based dynamical models to only the NIFS kinematics in order to limit other common systematic effects known to affect black hole mass measurements; namely degeneracies between the dark halo/the mass-to-light ratio/the black hole mass and the assumption of a stellar mass-to-light ratio that remains constant with radius. We note, however, that fitting dynamical models to the NIFS kinematics in combination with the large-scale HET kinematics, and in combination with the wide-field IFU PPAK kinematics, produces a black hole mass consistent with  $M_{\text{BH}} = (4.9 \pm 1.6) \times 10^9 M_{\odot}$ .

The black hole mass measurement presented here is a factor of  $\sim 3$  smaller than the best-fit masses previously reported by van den Bosch et al. (2012) and Yıldırım et al. (2015), both of which were determined from stellar-dynamical modeling of large-scale, seeing-limited spectroscopy. Neither study explicitly explored the effect of systematics on  $M_{\text{BH}}$ , which could significantly increase the range of plausible black holes

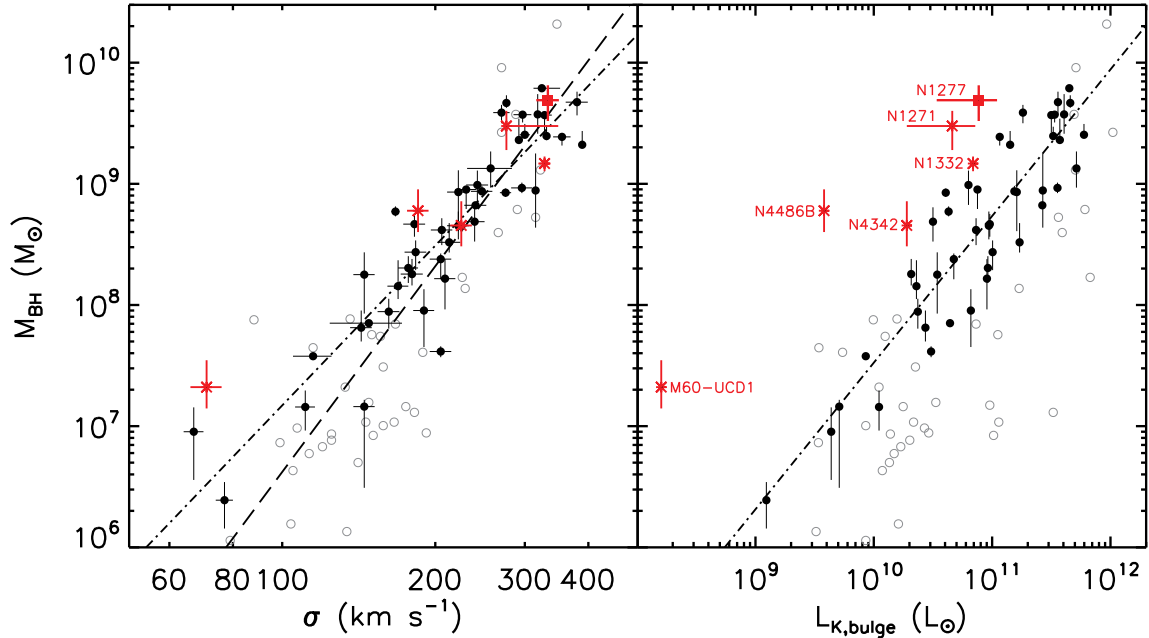


FIG. 5.— The location of NGC 1277 (red square) and other similar galaxies (red asterisks) on the black hole–host galaxy correlations. The  $\sim 80$  galaxies with dynamical black hole mass measurements shown here are taken from Kormendy & Ho (2013), with the exception of M60-UCD1 (Seth et al. 2014), NGC 1332 (Rusli et al. 2011), NGC 1271 (Walsh et al. 2015), and NGC 1277 (this work). The dot-dashed lines show the fitted relations from Kormendy & Ho (2013) to the black points. The gray points, composed largely of galaxies with pseudo-bulges, were excluded from the Kormendy & Ho (2013) fit. For comparison, the steeper dashed line is the relation from McConnell & Ma (2013), which was fit to nearly all points. NGC 1277 and the galaxies labeled in red have small sizes and large velocity dispersions for their galaxy luminosities, and they harbor over-massive black holes relative to  $M_{\text{BH}} - L_{\text{bul}}$  but are consistent with the  $M_{\text{BH}} - \sigma_*$  relation.

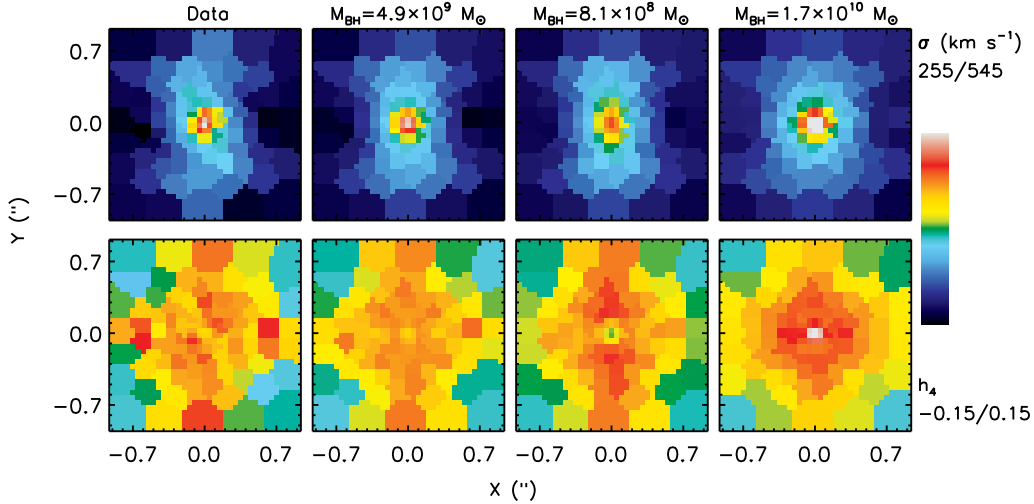


FIG. 6.— Comparison between the NIFS velocity dispersion and  $h_4$  (left) and the best-fit model with  $M_{\text{BH}} = 4.9 \times 10^9 M_{\odot}$  (middle left), a model with  $M_{\text{BH}} = 8.1 \times 10^8 M_{\odot}$  (middle right), and a model with  $M_{\text{BH}} = 1.7 \times 10^{10} M_{\odot}$  (right). A mass of  $8.1 \times 10^8 M_{\odot}$  is expected based on the  $M_{\text{BH}} - L_{\text{bul}}$  relation when conservatively using the galaxy’s total  $K$ -band luminosity of  $1.4 \times 10^{11} L_{\odot}$ , whereas a black hole mass of  $1.7 \times 10^{10} M_{\odot}$  is the previously published result from stellar-dynamical modeling of seeing-limited, large-scale spectroscopy (van den Bosch et al. 2012). When constructing the  $8.1 \times 10^8 M_{\odot}$  black hole model, we sample over mass-to-light ratios and dark halos as described in Section 7, and present the model with the lowest  $\chi^2$  for this black hole mass. The  $1.7 \times 10^{10} M_{\odot}$  black hole model uses the same mass-to-light ratio and dark halo found by van den Bosch et al. (2012). The best-fit model matches the observed velocity dispersion peak and slightly positive nuclear  $h_4$  values very well, however the smaller (larger) black hole under-predicts (over-predicts) the central velocity dispersion and  $h_4$  values.

masses. When instead considering the conservative lower  $3\sigma$  limit of  $6.5 \times 10^9 M_\odot$  from van den Bosch et al. (2012) and of  $4.0 \times 10^9 M_\odot$  from Yildirim et al. (2015), our result is consistent with the previous studies. Furthermore, our mass measurement agrees with the constraints found from rotating molecular gas. Scharwächter et al. (2015) presented unresolved CO(1-0) emission arising from the nuclear dust disk in NGC 1277, and found that both a  $\sim 5 \times 10^9 M_\odot$  and a  $\sim 1.7 \times 10^{10} M_\odot$  black hole are capable of reproducing the double-horned profile.

With  $M_{\text{BH}} = (4.9 \pm 1.6) \times 10^9 M_\odot$ , the black hole in NGC 1277 is one of the largest detected to date. NGC 1277 remains a positive outlier on the  $M_{\text{BH}} - L_{\text{bul}}$  relation, but is consistent with  $M_{\text{BH}} - \sigma_*$ . NGC 1277 is thought to be a relic of the  $z \sim 2$  massive quiescent galaxies (Trujillo et al. 2014; Ferré-Mateu et al. 2015), and could suggest that galaxies contained over-massive black holes at earlier epochs, such that the growth of black holes precedes the growth of their host galaxies.

Based on observations obtained at the Gemini Observa-

tory acquired through the Gemini Science Archive and processed using the Gemini IRAF package, which is operated by the Association of Universities for Research in Astronomy, Inc., under a cooperative agreement with the NSF on behalf of the Gemini partnership: the National Science Foundation (United States), the National Research Council (Canada), CONICYT (Chile), the Australian Research Council (Australia), Ministério da Ciência, Tecnologia e Inovação (Brazil) and Ministerio de Ciencia, Tecnología e Innovación Productiva (Argentina), under program GN-2011B-Q-27. Based on observations made with the NASA/ESA Hubble Space Telescope, and obtained from the Hubble Legacy Archive, which is a collaboration between the Space Telescope Science Institute (STScI/NASA), the Space Telescope European Coordinating Facility (ST-ECF/ESA) and the Canadian Astronomy Data Centre (CADAC/NRC/CSA). The authors acknowledge the Texas Advanced Computing Center (TACC; <http://www.tacc.utexas.edu>) at the University of Texas at Austin for providing HPC resources that have contributed to the research results reported within this paper. This research has made use of the NASA/IPAC Extragalactic Database which is operated by the Jet Propulsion Laboratory, California Institute of Technology, under contract with NASA.

## REFERENCES

- Bennett, V. N., Auger, M. W., Treu, T., Woo, J.-H., & Malkan, M. A. 2011, *ApJ*, 742, 107
- Boccas, M., Rigaut, F., Bec, M., et al. 2006, *Proc. SPIE*, 6272, 114
- Cappellari, M., & Copin, Y. 2003, *MNRAS*, 342, 345
- Cappellari, M., & Emsellem, E. 2004, *PASP*, 116, 138
- Cappellari, M., Neumayer, N., Reunanen, J., van der Werf, P. P., de Zeeuw, P. T., & Rix, H.-W. 2009, *MNRAS*, 394, 660
- Cretton, N., & van den Bosch, F. C. 1999, *ApJ*, 514, 704
- Daddi, E., Renzini, A., Pirzkal, N., et al. 2005, *ApJ*, 626, 680
- Dalla Bontà, E., Ferrarese, L., Corsini, E. M., et al. 2009, *ApJ*, 690, 537
- Decarli R., Falomo, R., Treves, A., Labita, M., Kotilainen, J. K., & Scarpa, R. 2010, *MNRAS*, 402, 2453
- de Francesco, G., Capetti, A., & Marconi, A. 2006, *A&A*, 460, 439
- Emsellem, E., Monnet, G., & Bacon, R. 1994, *A&A*, 285, 723
- Emsellem, E. 2013, *MNRAS*, 433, 1862
- Fabian, A. C. 1999, *MNRAS*, 308, L39
- Fabian, A. C., Sanders, J. C., Haehnelt, M., Rees, M. J., & Miller, J. M. 2013, *MNRAS*, 431, L38
- Falcón-Barroso, J., Sánchez-Blázquez, P., Vazdekis, A. 2011, *A&A*, 532, 95
- Ferrarese, L., & Merritt, D. 2000, *ApJ*, 539, L9
- Ferré-Mateu, A., Mezcuza, M., Trujillo, I., Balcells, M., & van den Bosch, R. C. E. 2015, *ApJ*, 808, 79
- Gebhardt, K., Bender, R., Bower, G., et al. 2000, *ApJL*, 539, L13
- Gebhardt, K., & Thomas, J. 2009, *ApJ*, 700, 1690
- Gebhardt, K., Adams, J., Richstone, D., et al. 2011, *ApJ*, 729, 119
- Gültekin, K., Richstone, D. O., Gebhardt, K., et al. 2009, *ApJ*, 698, 198
- Herriot, G., Morris, S., Anthony, A., et al. 2000, *Proc. SPIE*, 4007, 115
- Hill, G. J., Nicklas, H. E., MacQueen, P. J., Tejada, C., Cobos Duenas, F. J., Mitsch, W., 1998, *Proc. SPIE*, 3355, 375
- Jahnke, K., & Macciò, A. V. 2011, *ApJ*, 734, 92
- Jarrett, T. H., Chester, T., Cutri, R., Schneider, S., Skrutskie, M., & Huchra, J. P. 2000, *AJ*, 119, 2498
- Kelz, A., Verheijen, M. A. W., Roth, M. M., et al. 2006, *PASP*, 118, 129
- Kormendy, J., & Richstone, D. 1995, *ARA&A*, 33, 581
- Kormendy, J., Bender, R., Magorrian, J., et al. 1997, *ApJL*, 482, L139
- Kormendy, J., & Ho, L. C. 2013, *ARA&A*, 51, 511
- Krajnović, D., McDermid, R. M., Cappellari, M., & Davies, R. L. 2009, *MNRAS*, 399, 1839
- Krist, J., & Hook, R. 2004, *The Tiny Tim User's Guide* (Baltimore:STScI)
- Läsker, R., van den Bosch, R. C. E., van de Ven, G., et al. 2013, *MNRAS*, 434, L31
- Lauer, T. R., Tremaine, S., Richstone, D., & Faber, S. M. 2007, *ApJ*, 670, 249
- Marconi, A., & Hunt, L. K. 2003, *ApJ*, 589, L21
- Martín-Navarro, I., La Barbera, F., Vazdekis, A., Ferré-Mateu, A., Trujillo, I., & Beasley, M. A. 2015, *MNRAS*, 451, 1081
- McConnell, N. J., Ma, C.-P., Murphy, J. D., et al. 2012, *ApJ*, 756, 179
- McConnell, N. J., & Ma, C.-P. 2013, *ApJ*, 764, 184
- McConnell, N. J., Chen, S.-F. S., Ma, C.-P., Greene, J. E., Lauer, T. R., & Gebhardt, K. 2013, *ApJ*, 768, 21
- McGregor, P. J., Hart, J., Conroy, P. G., et al. 2003, *Proc. SPIE*, 4841, 1581
- Merloni, A., Bongiorno, A., Bolzonella, M., et al. 2010, *ApJ*, 708, 137
- Monnet, G., Bacon, R., & Emsellem, E. 1992, *A&A*, 253, 366
- Mould, J. R., Huchra, J. P., Freedman, W. L., et al. 2000, *ApJ*, 529, 786
- Navarro, J. F., Frenk, C. S., & White, S. D. M. 1996, *ApJ*, 462, 563
- Neumayer, N., Cappellari, M., Reunanen, J., Rix, H.-W., van der Werf, P. P., de Zeeuw, P. T., & Davies, R. I. 2007, *ApJ*, 671, 1329
- Onken, C. A., Valluri, M., Peterson, B. M., et al. 2007, *ApJ*, 670, 105
- Onken, C. A., Valluri, M., Brown, J. S., et al. 2014, *ApJ*, 791, 37
- Peng, C. Y., Impey, C. D., Rix, H.-W., et al. 2006, *ApJ*, 649, 616
- Peng, C. Y. 2007, *ApJ*, 671, 1098
- Peng, C. Y., Ho, L. C., Impey, C. D., & Rix, H.-W. 2010, *AJ*, 139, 2097
- Roth, M. M., Kelz, A., Fechner, T., et al. 2005, *PASP*, 117, 620
- Rusli, S. P., Thomas, J., Erwin, P., et al. 2011, *MNRAS*, 410, 1223
- Rusli, S. P., Thomas, J., Saglia, R. P., et al. 2013, *AJ*, 146, 45
- Salviander, S., & Shields, G. A. 2013, *ApJ*, 764, 80
- Salviander, S., Shields, G. A., & Bonning, E. W. 2015, *ApJ*, 799, 173
- Sánchez-Blázquez, P., Peletier, R. F., Jiménez-Vicente, J., et al. 2006, *MNRAS*, 371, 703
- Saulder, C., van den Bosch, R. C. E., & Mieske, S. 2015, *A&A*, 578, 134
- Scharwächter, J., Combes, F., Salomé, P., Sun, M., & Krips, M. 2015, submitted to *MNRAS*, arXiv:1507.02292
- Schulze, A., & Wisotzki, L. 2014, *MNRAS*, 438, 3422
- Seth, A. C., van den Bosch, R., Mieske, S., et al. 2014, *Natur*, 513, 398
- Shapiro, K. L., Cappellari, M., de Zeeuw, T., McDermid, R. M., Gebhardt, K., van den Bosch, R. C. E., & Statler, T. S. 2006, *MNRAS*, 370, 559
- Shen, S., Mo, H. J., White, S. D. M., et al. 2003, *MNRAS*, 343, 978
- Shen, Y., Greene, J. E., Ho, L. C., et al. 2015, 805, 96
- Shields, G. A., & Bonning, E. W. 2013, *ApJL*, 772, L5
- Silk, J., & Rees, M. J. 1998, *A&A*, 331, L1
- Trakhtenbrot, B., Urry, C. M., Civano, F., et al. 2015, *Science*, 349, 168
- Trujillo, I., Förster Schreiber, N. M., Rudnick, G., et al. 2006, *ApJ*, 650, 18
- Trujillo, I., Cenarro, A. J., de Lorenzo-Cáceres, A., Vazdekis, A., de la Rosa, I. G., & Cava, A. 2009, *ApJL*, 692, L118
- Trujillo, I., Ferré-Mateu, A., Balcells, M., Vazdekis, A., & Sánchez-Blázquez, P. 2014, *ApJL*, 780, L20
- Valdes, F., Gupta, R., Rose, J. A., Singh, H. P., & Bell, D. J. 2004, *ApJS*, 152, 251
- van den Bosch, R. C. E., van de Ven, G., Verolme, E. K., Cappellari, M., & de Zeeuw, P. T. 2008, *MNRAS*, 385, 647
- van den Bosch, R. C. E., & de Zeeuw, P. T. 2010, *MNRAS*, 401, 1770

- van den Bosch, R. C. E., Gebhardt, K., Gültekin, K., et al. 2012, *Nature*, 491, 729
- van den Bosch, R. C. E., Gebhardt, K., Gültekin, K., Yıldırım, A., & Walsh, J. L. 2015, *ApJS*, 218, 10
- van der Wel, A., Rix, H.-W., Wuyts, S., et al. 2011, *ApJ*, 730, 38
- van der Wel, A., Franx, M., van Dokkum, P. G., et al. 2014, *ApJ*, 788, 28
- van Dokkum, P. G., Kriek, M., & Franx, M. 2009, *Nature*, 460, 717
- van Dokkum, P. G., Whitaker, K. E., Brammer, G., et al. 2010, *ApJ*, 709, 1018
- Verheijen, M. A. W., Bershadsky, M. A., Andersen, D. R., et al. 2004, *AN*, 325, 151
- Walsh, J. L., van den Bosch, R. C. E., Barth, A. J., & Sarzi, Marc. 2012, *ApJ*, 753, 79
- Walsh, J. L., Barth, A. J., Ho, L. C., & Sarzi, M. 2013, *ApJ*, 770, 86
- Walsh, J. L., van den Bosch, R. C. E., Gebhardt, K., et al. 2015, *ApJ*, 808, 183
- Wellons, S., Torrey, P., Ma, C.-P., et al. 2015, submitted to *MNRAS*, arXiv:1507.02291
- Winge, C., Riffel, R. A., & Storchi-Bergmann, T. 2009, *ApJS*, 185, 186
- Woo, J.-H., Treu, T., Malkan, M. A., & Blandford, R. D. 2008, *ApJ*, 681, 925
- Yıldırım, A., van den Bosch, R. C. E., van de Ven, G., et al. 2015, *MNRAS*, 452, 1792